RSC Advances

PAPER

View Article Online
View Journal | View Issue

Cite this: *RSC Adv.*, 2020, **10**, 22311

Effect of iron doped titanium oxide encapsulated in alginate on photocatalytic activity for the removal of dye pollutants

Soulaima Chkirida,[ab] Nadia Zari,[a] Redouane Achour,[b] Abou el kacem Qaiss [a] and Rachid Bouhfid *[a]

The focal point of this work is the design and comparison of two types of iron doped TiO_2 prepared by a simple sol–gel method and then encapsulated in an alginate matrix. The as-prepared recyclable bio-nanocomposite photocatalysts were made of different amounts of TiO_2-Fe_2O_3 and TiO_2-Fe_3O_4 (1%, 2.5%, 5%, and 10%) and were developed to improve the photocatalytic efficiency of TiO_2 and simultaneously to achieve an expanded visible-light response range with high visible-light absorption potential in order to degrade organic pollutants from aqueous solutions, as a potential application. As it is essential to characterize a material to better understand it, accurate characterization of the resulting bio-nanocomposites was carried out using X-ray diffraction (XRD), scanning electron microscopy coupled to energy dispersive X-ray spectroscopy (SEM-EDX), Fourier transform infrared spectroscopy (FTIR) and UV-diffuse reflectance spectroscopy (UV-DRS). In this study, the emphasis on blending the alginate and the iron doped-TiO_2 photocatalyst nanoparticles results in a multicomponent particular shaped system that exhibits a porous structure, an exceptional surface area and a smaller band gap due to the presence of iron nanoparticles that could also maintain e^-/hole separation for better photocatalytic activity under visible light.

Received 30th March 2020
Accepted 28th May 2020

DOI: 10.1039/d0ra02898c

rsc.li/rsc-advances

Introduction

Many conventional physicochemical technologies have been used for many years, and are still used, for the removal of organic contaminants, and examples include: coagulation–flocculation, adsorption, membrane technologies of, and ion exchange. However, these traditional methods only transfer organic compounds from the liquid to the solid phase, which then requires further treatment and involves regeneration of the adsorbent or membrane replacement, increasing the overall treatment costs.

Similarly, there has been a lot of interest in photocatalysis, which is a widespread advanced oxidation process that has been used in various water decontamination treatments for inorganic and organic pollutant elimination, because of its ability to mineralize organic compounds into non-toxic products, and its energy-efficiency, and cost-effectiveness.

For this purpose, titanium dioxide (TiO_2) is an excellent photocatalyst with a significantly high photocatalytic activity under ultraviolet (UV) light irradiation, which also has good chemical stability, low cost and low toxicity.[1] However, practical applications of TiO_2 nanoparticles (NPs) are restricted by the difficulties in separating and recycling them after photocatalytic reactions, and by their ability of absorbing only in the near UV region ($\lambda < 387$ nm). The TiO_2 NPs also show a weak capacity to absorb the solar irradiation fraction (<5%)[2] which prompted many researchers to try to extend its absorption wavelength to the visible light edge ($\lambda > 400$ nm) to afford a broad absorption range, and thus, boosting the photocatalytic activity of TiO_2.

The main solution to stretching out the TiO_2 absorption in the visible light region and to change its photocatalytic activity is doping with different elements such as metals and non metals.[3,4] Doping of semiconductors involves shortening the band-gap level by decreasing the conduction band, which prevents the recombination of electron–hole pairs.[5] Similarly, much research has been published on the doping of metallic NPs and their enhancement of catalysis performance[6,7] as well as the improvement of their antibacterial efficacy.[8,9] Moreover, other studies have described and confirmed that mixed TiO_2-based catalysts consisting of iron oxides such as Fe_2O_3 or Fe_3O_4 had an advantageous effect on the photocatalytic performance when compared with the use of undoped TiO_2.[5,10]

Because photocatalytic degradation takes place on the surface of the photocatalyst, adsorption capacities are very important for the accumulation of the pollutants onto the surface of the photocatalyst for effective degradation. Recently,

[a]*Moroccan Foundation for Advanced Science, Innovation and Research (MAScIR), Composites et Nanocomposites Center, Rabat Design Center, Rue Mohamed El Jazouli, Madinat El Irfane, 10100 Rabat, Morocco. E-mail: r.bouhfid@mascir.com*
[b]*Laboratoire de Chimie Organique et Hétérocyclique, Faculty of Science, Mohammed V-Rabat University, Rabat, Morocco*

iron oxides have been proved to be a good adsorbent[11,12] but not sufficiently good because TiO_2 has poor affinity for organic pollutants and relatively low adsorption abilities. In addition to other shortcomings like their tendency to agglomerate because of the instability of the particles at nanoscale sizes and the difficulty of getting them distributed uniformly, which may reduce their surface area and impede the incidence of light and inevitably diminish their photocatalytic efficiency.[13] In addition this is all without considering the major challenge of separation and recovery after treatment.[14]

To overcome these drawbacks and boundaries cited previously which hinder the application at large scale, a good approach seems to be to introduce a new material to the system with a good adsorption capacity as a support by imbedding the nanosized particles of the photocatalyst in it. Among the best candidates for this purpose are biopolymers, because they are plentiful, inexpensive and eco-friendly due to their biodegradability. The use of alginate in this work as a support material for iron oxide doped TiO_2 provides a porous structure, which permits selective adsorption of organic pollutants, because of their electrical charge and their interaction with the negative carboxylate groups of the alginate; it also permits the stabilization of the NPs for easy recovery. This biopolymer is a natural polysaccharide found in marine brown algae. It consists of a linear structure with repeating units of: mannuronate (M), guluronate (G) and mannuronate–guluronate with proportions which differ with the source of the biopolymer.[15] Among the good properties of the alginate matrix, are its viscosity and the ability to form and stabilize gels that enable a good water holding capacity and the ability of entrapping reinforcements within its three-dimensional network by the formation of hydrogels resulting in a significant mechanical strength. Hence, a range of applications have adopted the use of this up-and-coming biopolymer, notably in the pharmaceutical, cosmetics, food and industrial fields.[15,16]

Herein the focus is first and foremost to accentuate and emphasize the design, followed by the preparation and characterization of new bio-nanocomposites based on iron oxide doped TiO_2 encapsulated in a versatile biopolymer in the form of beads. This microsphere shape results in multiple benefits resulting from their mechanical consistency and their large size (3–4 mm) that facilitate the task of their dispersion in polluted solutions and then recovering them. In addition, they have a very high porosity that imparts the improved functionalities of these hydrogels, for example, enhanced adsorption capacities.

The ability of these as prepared materials in the adsorption/degradation of toxins and water pollutants under UV irradiation and visible light will be determined through use of multiple tests in UV and visible light in upcoming studies.

Experimental section

Materials and reagents

Titanium(IV) butoxide (97%), Fe_3O_4 NPs, methylene blue (MB), calcium chloride dehydrate ($CaCl_2 \cdot 2H_2O \geq 99\%$), and nitric acid ($HNO_3$) for adjusting the pH were purchased from Sigma-Aldrich. Alginic acid sodium salt (pharmaceutical grade) and isopropanol solvent were purchased from CARLO ERBA. Ultrapure water, which was essential for all the experiments, was obtained from a Milli-Q system (18.2 mΩ cm, Millipore).

General process of the preparation of alginate-modified TiO_2 hydrogel microspheres

An transparent homogeneous gel of alginate was made by dissolving 1 g of alginate in 40 ml of deionized water with vigorous stirring for 3 h to guarantee complete dissolution.

The TiO_2-Fe_2O_3 (3 : 1) nanocomposite was prepared *via* a sol gel method in acidic medium (pH = 3). The titanium precursor: tetrabutoxide of titanium (TBT, 5 ml) was mixed with 15 ml of isopropanol at room temperature under vigorous stirring for 1 h (Solution A). An amount of Fe_3O_4 was dispersed in 250 ml of acidic distillated water (pH = 3), and sonicated for 45 min (Branson Sonifier Ultrasonic mixer) (Solution B). Solution B was then added dropwise to Solution A, under vigorous stirring. Then it was heated under reflux up to 60–70 °C for almost 20 h to allow the hydrolysis–condensation reaction of the precursor of titanium to complete, and the gel to form. Then the gel was dried in an oven at 100 °C for several hours until a dark grey powder was obtained. To promote the development of the TiO_2 NPs (anatase and rutile) the resulting dark powder was calcinated at a temperature of 650 °C for 3 h. After calcination, a reddish-brown powder was obtained which indicated the transition of Fe_3O_4 to Fe_2O_3 had occurred.

Various amounts of TiO_2-Fe_2O_3 oxide were dispersed in distilled water and sonicated for 30 min using a sonication apparatus to ensure good dispersion. Then these suspensions were gradually added to the alginate solution with TiO_2-Fe_2O_3 oxide contents of (1%, 2.5%, 5% and 10%), followed by stirring at ambient temperature for 3 h until the formation of a homogeneous, well dispersed gel. One sample of TiO_2-Fe_2O_3-alginate was synthesized with a fixed structure and different concentrations of photocatalyst.

The homogenous TiO_2-Fe_2O_3-alginate solutions were added dropwise through a syringe needle into a bath containing 4% $CaCl_2$ solution with an ideal drop height of 12 cm to obtain spherical pearls. The bath stayed transparent due to the cross-linking of alginate's interfacial chains by calcium ions, which induced the formation of a protective layer that stopped the reinforcement disappearing out of the matrix. After a maturation time of 4 h, the resulting bio-nanocomposite microspheres were filtered, and then washed well with distilled water to remove the excess calcium and stored wet in a water bath to prevent the breaking and the collapse of their internal structures.

For comparison purposes, TiO_2-Fe_3O_4-alginate oxides were also prepared following a solid method. Indeed, the TiO_2 NPs previously prepared *via* Solution A and Fe_3O_4 were adequately ground and homogenized in a mortar with the same weight ratio of 3 : 1 until a grey well-ground homogeneous powder was obtained. The mixed ground powder was dispersed in distilled water and sonicated for 30 min. Afterwards, it was added in increasing amounts to the alginate solution with TiO_2-Fe_3O_4 contents of (1%, 2.5%, 5% and 10%) and the hydrogel beads were developed as described previously.

The resulting bio-nanocomposite hydrogels were stored in aqueous solution to prevent any moisture degradation, and were denoted as: Alg-TiO_2 : Fe_3O_4-*X*% and Alg-TiO_2 : Fe_2O_3-*X*%, where *X* indicates the amount of TiO_2-Fe_3O_4 and TiO_2-Fe_2O_3 in the alginate matrix, respectively.

For any characterization purposes, the moisture should be removed from the samples, which ensures the transition of hydrogels to cryogels, due to the high porosity and extremely low weight which allows the preservation of the textural properties and allows the maximum amount of information to be gathered. For this purpose, freeze-drying of hydrogel beads was assessed at 218 K. The interstitial solvent (water) underwent a sublimation in the freeze dryer (Christ Alpha 2-4 LDplus).

Characterization methods

The Alg-TiO_2-Fe_2O_3 and Alg-TiO_2-Fe_3O_4 hydrogel microspheres were photographed, using a digital camera, to highlight and illustrate their structure. The morphologies of the cryogel's surface were viewed using a scanning electron microscope (ThermoFisher Scientific™ Quattro ESEM) after coating with a layer of carbon. In order to display their internal structure, a sharp razor was used to prepare the cross-section of the as-prepared cryogels. For a complete study, an energy dispersive X-ray spectroscope (EDX) was attached to a large field detector and was used to verify the elemental composition of the cryogels and to acquire the compositional maps.

The functional groups of alginate, TiO_2 and iron oxides and the structure of the bio-nanocomposites were investigated by FTIR spectroscopy using a FTIR spectrometer (Bruker Vertex 70). The X-ray diffractions measurements were obtained using an XRD diffractometer (PANalytical X'PERT Pro MPD) using Cu Kα radiation at 45 kV and 40 mA in the range from 10° to 90° (2θ), and the identification of crystalline structures was done using the library of the Joint Committee on Powder Diffraction Standards (JCPDS). Diffuse reflectance UV-Vis (UV-DRS) spectra were recorded on a spectrophotometer (PerkinElmer LAMBDA 1050 UV/Vis/NIR) in the wavelength range of 200 to 800 nm.

Results and discussion

Morphology/size of the bio-nanocomposites

The as prepared bio-nanocomposites were monodisperse spherical beads, with a diameter in the range of 3–4 mm. The reason for choosing the round shape was because a sphere allowed pollutant diffusion to the core in all directions, besides providing the lowest surface area-to-volume ratio of all of geometric figures which was another important aspect.[17] As Fig. 1 shows, the more the shape of the spherical beads was reinforced with photocatalyst NPs, the darker their color became.

Diffuse reflectance spectroscopy

Optical properties are pivotal and crucial characteristics for a catalyst's activity in photocatalysis. For this purpose, UV-Vis DRS analysis was used to gain insight into the photocatalysts interaction with photons and to determine their band gap energy. The measurement of optical absorption was done in the range of 200–800 nm.

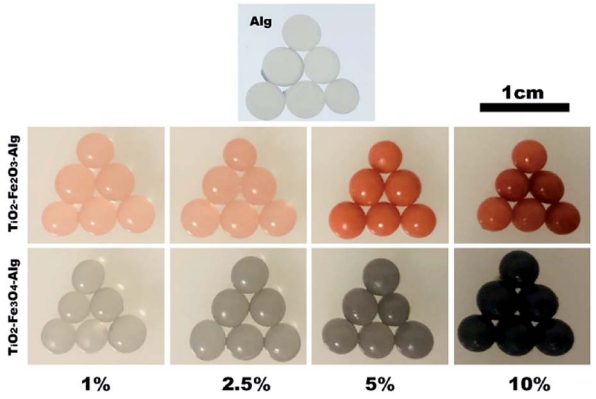

Fig. 1 Sizes/shapes and colors of the bio-nanocomposites.

Fig. 2 shows the diffused scattering UV-Vis spectra for the three samples. It shows that the absorption of pure TiO_2 was positioned at a light wavelength of about 390 nm, revealing the insignificant absorbance of TiO_2 in the visible region. The modification of TiO_2 with iron oxides: Fe_2O_3 and Fe_3O_4, successfully extended and prolonged the absorption to the visible light region by a shift to a longer wavelength from 440 nm for pure TiO_2 to 575 nm and 700 nm for TiO_2-Fe_3O_4 and TiO_2-Fe_2O_3, respectively, indicating that iron-TiO_2 catalysts have a promising potential for photocatalysis degradation within the visible light spectrum. These results were in agreement with other work already done with the aim of doping TiO_2 with iron oxides.[5,18] An accurate determination of the band gap energy is also necessary because it is a decisive characteristic in terms of determining the electronic structure of materials especially in the case of doping. It is also important that the type of band-to-band transition in these synthesized catalysts should be established. The absorption data were fitted to direct and indirect bandgap transition equations using the Tauc plot method

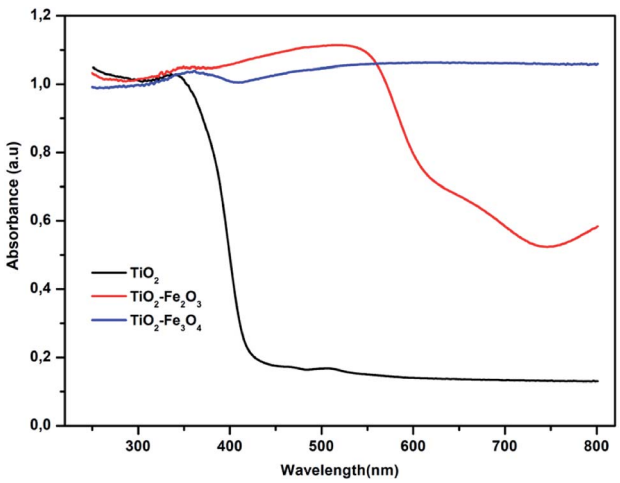

Fig. 2 UV-Vis diffuse reflectance spectra of catalysts.

which consisted of linking the optical absorption coefficient α to the gap energy, E_g, from the equation:

$$(\alpha h\nu)^n = K(h\nu - E_g)$$

Where $h\nu$ (eV) is the incident photon energy, α (cm^{-1}) is the absorption coefficient, K is the energy independent constant and n is the electronic transition coefficient, which is 2 for an allowed indirect transition and 0.5 for an allowed direct transition. Fundamentally, by plotting the intersection of the straight-line fit of the zone associated to the edge of optical absorption and the $h\nu$-axis the gap energy is obtained (the value of $h\nu$ extrapolated to $\alpha = 0$). In point of fact, this a tested, proved and accurate method when carried out satisfactorily.[19]

Investigations have revealed that a transition of $n = 2$, is the most accurate and the Tauc plot equation gives the best linear fit which was in agreement with similar results in other published papers (as shown in Fig. 3).[20]

The band gap calculated for pure TiO_2 was 2.9 eV and for Fe_2O_3-doped TiO_2 and Fe_3O_4-doped TiO_2 NPs were 1.80 and 1.88 eV respectively. It was quite obvious that the presence of iron oxides: Fe_2O_3 and Fe_3O_4, in the photocatalyst structures decreased the band gap of both TiO_2-Fe_2O_3 and TiO_2-Fe_3O_4 revealing the potential for using these compounds in photocatalysis degradation in the visible light spectrum.

This was attributable to the intermediate states' generation between the valence and conduction bands of TiO_2 with the incorporation of iron oxides, which were responsible for the band gap decrease. This could be the main reason for the improved visible light absorption.

XRD analysis

The XRD analysis was carried out to inspect the crystalline morphologies and phases of the as-prepared materials in the range of 10°–90° and the results are shown in Fig. 4.

Fig. 4 displays the diffraction peaks (2θ) of pure TiO_2 at: 25.31°, 37.52°, 47.90°, 53.90°, 56.29°, 62.66°, 69.04° and 74.68°

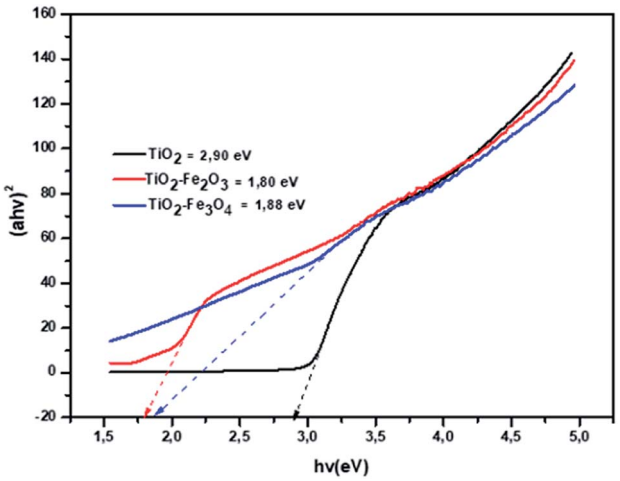

Fig. 3 Tauc plots for energy band gap calculations of pure TiO_2, Fe_2O_3-doped TiO_2 and Fe_3O_4-doped TiO_2 photocatalysts for $n = 2$.

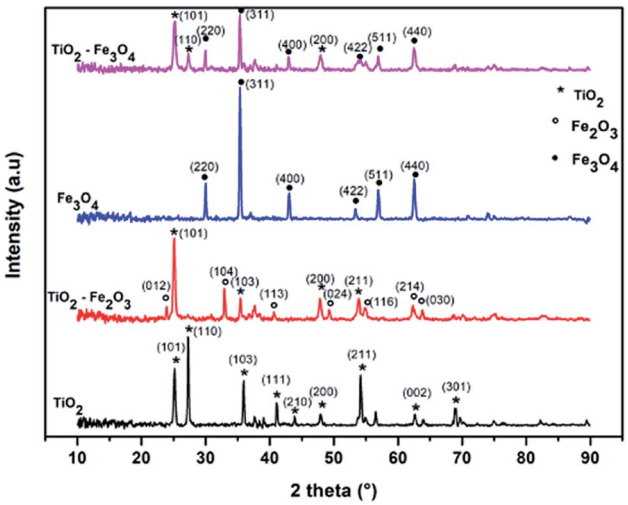

Fig. 4 The XRD patterns of bare TiO_2, Fe_3O_4, and Fe_2O_3 doped TiO_2.

which were attributed to the anatase phase and at: 27.67°, 35.52°, and 56.30° that corresponded to the rutile phase according to standard XRD pattern of TiO_2 (JCPDS 21-1272)[21]. These peaks were sharp and intense, demonstrating the well-crystallized structure of the prepared TiO_2. Fig. 4 also shows that the mixed oxide phase: TiO_2-Fe_2O_3 has been formed. In fact, the diffraction peaks corresponding to TiO_2, discussed previously, are present beside the Fe_2O_3 peaks that were indexed to the crystal phase of hematite. The main diffraction peaks of Fe_2O_3 were observed at 2θ of: 24.03°, 33.50°, 36.4°, 40.25°, 48.80°, 57.73°, 61.74° and 65.02° (JCPDS card no. 00-001-1053)[22]. This indicated that the TiO_2 NPs were generated *in situ* on the surface of Fe_3O_4 particles, due to the hydrolysis of TBT, before it changes into Fe_2O_3 through annealing. Similarly, for TiO_2-Fe_3O_4 binary mixed oxides generated by the solid path without annealing, the coexistence was also verified. As presented in Fig. 4, in addition to the TiO_2 peaks, the diffraction peaks at 2θ: 30.05°, 35.32°, 42.97°, 53.36°, 57.00° and 62.29° were verified to be consistent with those of the standard XRD pattern of Fe_3O_4 (JCPDS file no. 19-0629)[23]. After the encapsulation of these NPs on the biopolymer matrix, the intensity of the characteristic peaks of TiO_2 and the iron oxides were obviously reduced or hidden due to the shielding effect of alginate, which was typical, because it exhibited the characteristic of amorphous polymers and in this case consists of over 80% of bio-nanocomposites.[24]

Table 1 displays the crystallite size of the as-prepared NPs and mixed oxides obtained using the Scherrer–Debye equation. The crystallite size of all the samples was within the range of 25–31 nm. It is worth noting that no notable increase in the particle's size was detected either for TiO_2-Fe_3O_4 generated by a solid path or for TiO_2-Fe_2O_3, which proved that the stability of the solid was maintained even after the addition of iron oxide NPs.

FTIR spectra

For qualitative identification, investigation of the functional groups, and to confirm the high purity of the products formed,

Table 1 Crystallite size of nanoparticles calculated from Scherrer–Debye equation

Sample	Average crystallite size (nm)
TiO_2	31.14
Fe_3O_4	30.91
TiO_2-Fe_2O_3	25.44
TiO_2-Fe_3O_4	28.53

FTIR analysis in the range of 400–4000 cm^{-1} was used. Fig. 5 shows the FTIR spectra of pure TiO_2, TiO_2-Fe_2O_3 and TiO_2-Fe_2O_3-Alg. In addition, it also depicts the nanocomposites of TiO_2-Fe_3O_4 and TiO_2-Fe_3O_4-Alg.

The broad absorption band around 3200–3500 cm^{-1} can be attributed to the stretching vibration of –OH from the hydroxyl group.[25] The absorption bands at 2931 and 2917 cm^{-1}, were associated with the –C–H stretching vibration. Whereas the characteristic bands of both asymmetric and symmetric stretching vibrations of the COO^- groups at 1588 and 1403 cm^{-1} in Fig. 5, were indicative of alginate. Characteristic broad bands were also found at 1593–1620 cm^{-1} and these were the hydroxyl groups from the physically adsorbed water on the beads' surface (Fig. 5). The presence of these radicals may prove vital during the photocatalytic process. It has been shown by results of previous studies that the presence of physically adsorbed water on catalyst surface increases the oxidizing power of the photocatalysts' system,[26] and this happens because the hydroxyl group present at the catalyst surface could react with the photo excited holes during the reaction to form hydroxyl radicals,[27] which was consistent with the work of Nadimi *et al.*[28] It is well known that most of the important bands of TiO_2 and iron oxides are observed below 800 cm^{-1}. The absorption bands in the region of 500 and 440 cm^{-1} shown in Fig. 5 confirmed the presence of stretching vibrations of –Fe–O– in addition to those of –Ti–O– which occurred between 420 and 470 cm^{-1}. In fact, previous research by Choi *et al.*[29] showed that peaks between 400–750 cm^{-1} were associated with Ti–O vibrations which confirmed the formation of TiO_2. Thus, TiO_2 NPs were successfully modified with iron oxides. The low percentages of iron oxides in the as-prepared bio-nanocomposites, as shown in EDX analysis, the absorption bands cannot be credibly determined or well resolved.

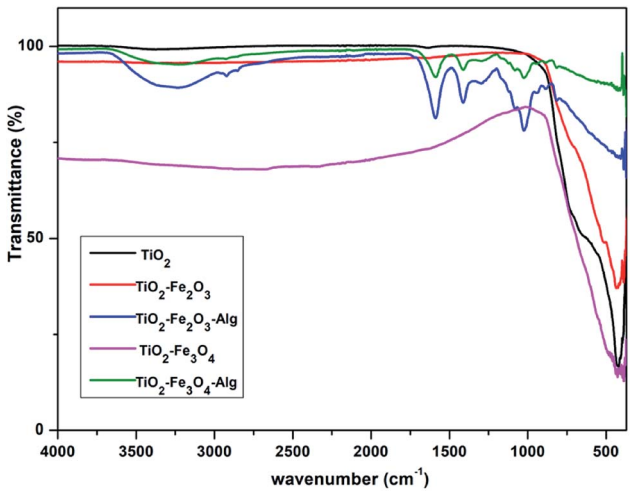

Fig. 5 The FTIR spectra of bare TiO_2, iron oxide doped TiO_2 and the bio-nanocomposites.

Morphology analysis by SEM-EDX

For cryogel preparation, a freeze-drying method was used in order to maintain the porous internal structure. The cross section of the two bio-nanocomposite cryogels made it possible to visualize the porous internal surface and its appearance, as shown in Fig. 6a and b. In fact, the biopolymer cross-sectional micrographics show spongy macroscopic networks with many holes and interconnected pores because of the uniform embedding and filling with well dispersed photocatalyst particles. This interconnected honeycomb-like structure and high homogeneous porosity was due to the overlapped NPs between

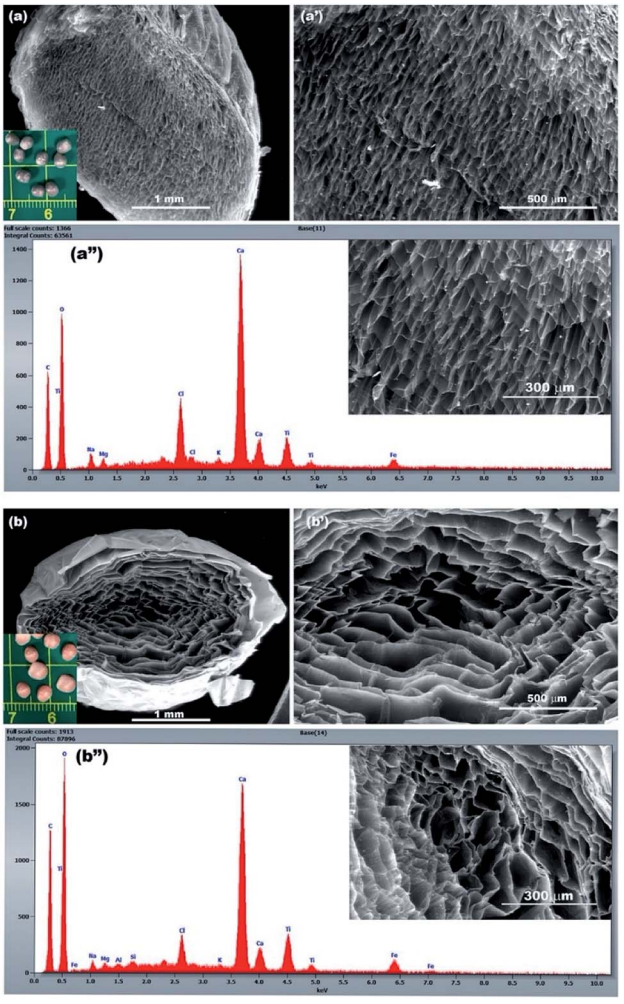

Fig. 6 SEM-EDX micrographs of the as prepared bio-nanocomposite beads: TiO_2-Fe_3O_4-Alg (a, a′ and a″) and TiO_2-Fe_2O_3-Alg (b, b′ and b″).

the fibrils of the biopolymer which facilitate the solution diffusion, the pollutants' adsorption and then its removal. The presence of photocatalyst NPs were confirmed by the results of the EDX analysis. Fig. 6a″ and b″ show, as expected, the presence of the titanium element (Ti) as well as the iron (Fe) which confirmed the entrapping of TiO_2 and the iron doped TiO_2 within the biopolymeric matrix.

From all these results, it can be seen that the unique microstructure of these bio-nanocomposites makes them outstanding materials for water purification applications.

Adsorption testing of the bio-nanocomposites

Because there were four different percentages per composite, it was deemed useful to execute some preliminary evaluation and assessment in terms of the uptake efficiency of a pollutant model (methylene blue) as shown in Fig. 7. For the batch experiments, 100 ml of MB solutions of prearranged initial concentrations (40–100 mg l^{-1}) were mixed with exactly 3 g of photo-catalyst hydrogel (which corresponded to 0.1 g of dry matter) in suitable flasks. Agitation of the solution was continued until equilibrium was attained. The monitoring of the reaction was carried out by withdrawing samples from the solutions at specific time intervals, then the supernatant's concentration was determined by UV-Vis spectrometry (Shimadzu UV-1900) at $\lambda_{max} = 664$ nm. A reaction time of 2 h was preferred as the appropriate time for testing the potential and effectiveness of the adsorption process.

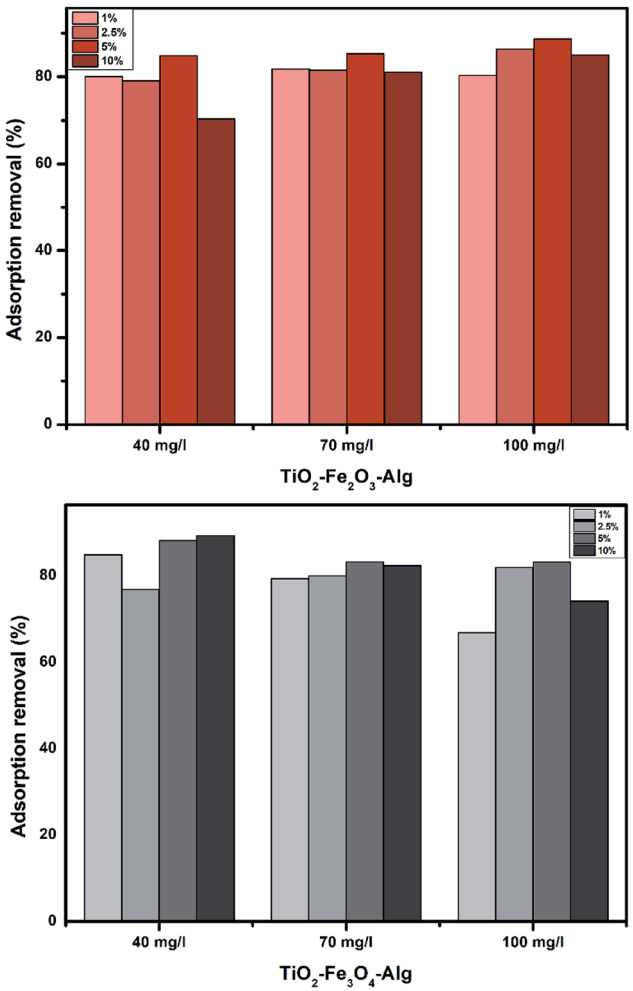

Fig. 7 Selection of the best bio-nanocomposites from the adsorption tests using three different initial concentrations.

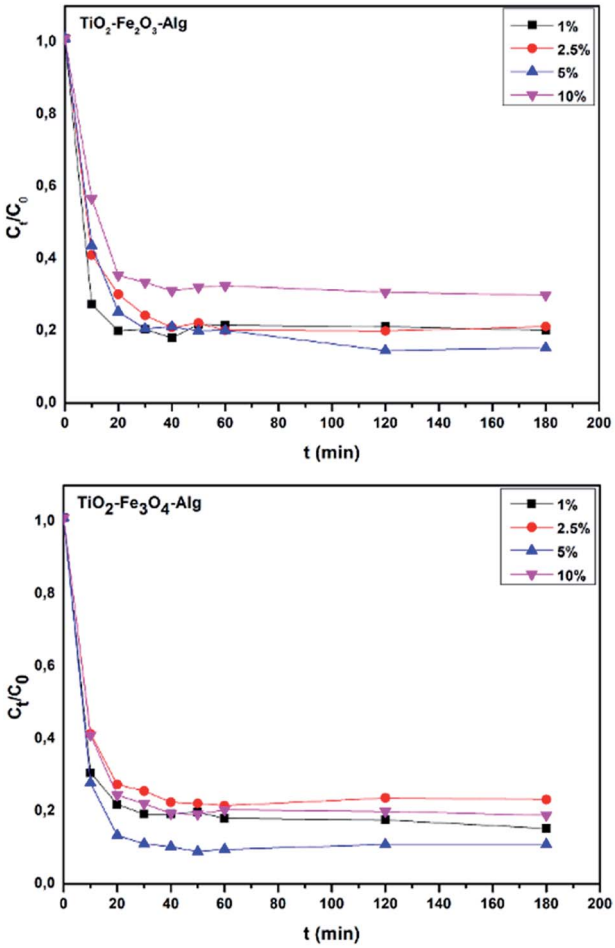

Fig. 8 C_t/C_0 plots *versus* time for the two best bio-nanocomposites.

The results of the dye removal observations using the prepared samples is shown in Fig. 7 and 8, which confirmed that out of all the samples tested, TiO_2-Fe_2O_3-Alg-5% and TiO_2-Fe_3O_4-Alg-5% were the best adsorbents. The MB removal (%) was calculated by the formula given below:

$$\%\ \text{Adsorption removal} = \frac{(C_0 - C_t)}{C_0} \times 100$$

where C_0 is the initial concentration and C_t is the concentration at time t. Against this background, all further tests would be carried out using these bio-nanocomposites.

Conclusions

The TiO_2 photocatalyst was successfully modified with iron oxides, and incorporated into alginate hydrogels. The alginate can provide the composites with a strengthened mechanical

structure, as well as a uniform porosity, and is a promising candidate to facilitate the recovery of the photocatalyst from the reaction medium. Based on UV-DRS characterization results, the doping of TiO_2 nanoparticles with Fe_2O_3 and Fe_3O_4 iron oxides widens the light absorption region towards the visible region by decreasing the band gap energies and shifting them to higher wavenumbers. Hence, these bio-nanocomposites are suitable for the photodegradation of dissimilar organic pollutants under UV irradiation as well as visible light. Moreover, the simplicity of the preparation methods of both TiO_2-Fe_2O_3-Alg and TiO_2-Fe_3O_4-Alg indicates that these bio-nanocomposites would be advantageous in the dye wastewater sector.

Conflicts of interest

There are no conflicts to declare.

Acknowledgements

This work was supported by MAScIR, Moroccan Foundation for Advanced Science, Innovation and Research.

Notes and references

1 L. G. Devi, B. N. Murhty and S. G. Kumar, *Catal. Lett.*, 2009, **130**, 496–503.
2 S. Yin, Q. Zhang, F. Saito and T. Sato, *Chem. Lett.*, 2003, **32**, 358–359.
3 R. Asahi, T. Morikawa, T. Ohwaki, K. Aoki and Y. Taga, *Science*, 2001, **293**, 269–271.
4 D. Chen, Z. Jiang, J. Geng, Q. Wang and D. Yang, *Ind. Eng. Chem. Res.*, 2007, **46**, 2741–2746.
5 N. Abbas, G. N. Shao, M. S. Haider, S. M. Imran, S. Soo and H. Taik, *J. Ind. Eng. Chem.*, 2016, **39**, 112–120.
6 U. Qumar, M. Ikram, M. Imran, A. Haider, A. Ul-Hamid, J. Haider, K. N. Riaz and S. Ali, *Dalton Trans.*, 2020, **42**, 5362–5377.
7 J. Hassan, M. Ikram, M. Imran, M. Aqeel and S. Ali, *Nanoscale Res. Lett.*, 2020, **15**, 75.
8 M. Ikram, S. Abbasi, A. Haider, S. Naz, A. Ul-Hami, M. Imran, J. Haider and A. Ghaffar, *Nanotechnology*, 2020, **31**, 275704.
9 M. Aqeel, M. Ikram, A. Asghar, A. Haider, A. UI-Hamid, M. Imran and S. Ali, *Appl. Nanosci.*, 2020, **10**, 2045–2055.
10 S. Xuan, W. Jiang, X. Gong, Y. Hu and Z. Chen, *J. Phys. Chem. C*, 2009, **113**, 553–558.
11 B. L. Zhong, J. Hu, H. Liang, A. Cao, W. Song and L. Wan, *Adv. Mater.*, 2006, **18**, 2426–2431.
12 L. Wan, K. Shi, X. Tian and H. Fu, *J. Solid State Chem.*, 2008, **181**, 735–740.
13 S. Mallakpour and E. Nikkhoo, *Adv. Powder Technol.*, 2013, **25**, 348–353.
14 J. Cui, T. He and X. Zhang, *Catal. Commun.*, 2013, **40**, 66–70.
15 C. Ouwerx, N. Velings, M. M. Mestdagh and M. A. V. Axelos, *Polym. Gels Networks*, 1998, **6**, 393–408.
16 S. N. Pawar and K. J. Edgar, *Biomaterials*, 2012, **33**, 3279–3305.
17 I. M. Bjørge, A. M. S. Costa, A. Sofia Silva, J. P. O. Vidal, J. Miguel Nóbrega and J. F. Mano, *Soft Matter*, 2018, **14**, 5622–5627.
18 X. Dai, G. Lu, Y. Hu, X. Xie, X. Wang and J. Sun, *Ceram. Int.*, 2019, **45**, 13187–131922.
19 B. D. Viezbicke, S. Patel, B. E. Davis and D. P. B. Iii, *Phys. Status Solidi B*, 2015, **252**, 1700–1710.
20 R. Lopez and R. Gomez, *J. Sol–Gel Sci. Technol.*, 2012, 1–7.
21 C. Wang, H. Shi and Y. Li, *Appl. Surf. Sci.*, 2011, **257**, 6873–6877.
22 S. Hong-xia, Y. A. O. Jian-lin and G. U. Ren-ao, *Trans. Nonferrous Met. Soc. China*, 2009, **19**, 652–656.
23 Y. Wei, B. Han, X. Hu and Y. Lin, *Procedia Eng.*, 2012, **27**, 632–637.
24 D. Kanakaraju, N. Rusydah, Y. Lim and A. Pace, *Sustainable Chem. Pharm.*, 2018, **8**, 50–62.
25 L. Cordero-arias, A. R. Boccaccini and S. Virtanen, *Surf. Coat. Technol.*, 2015, **265**, 212–217.
26 Z. Ding, G. Q. Lu and P. F. Greenfield, *J. Phys. Chem. B*, 2000, **104**, 4815–4820.
27 F. Pelletier and B. Thiébaut, *Johnson Matthey Technol. Rev.*, 2016, **60**, 39–54.
28 M. Nadimi, A. Z. Saravani, M. A. Aroon and A. E. Pirbazari, *Mater. Chem. Phys.*, 2018, **225**, 464–474.
29 S. Choi, B. Chu, S. G. Lee, S. W. Lee, S. S. Im, S. H. Kim and J. K. Park, *J. Sol-Gel Sci. Technol.*, 2004, **30**, 215–221.